

High-precision determination of the frequency-shift enhancement factor in Rb-¹²⁹Xe

A. I. Nahlawi and Z. L. Ma*

Department of Physics and Astronomy, University of Utah, 115 South 1400 East, Salt Lake City, Utah 84112-0830, USA

M. S. Conradi

ABQMR, 2301 Yale Boulevard S.E., Suite C-2, Albuquerque, New Mexico 87106, USA

B. Saam†

Department of Physics and Astronomy, Washington State University, P.O. Box 642814, Pullman, Washington 99164-2814, USA

 (Received 25 April 2019; revised manuscript received 24 October 2019; published 22 November 2019)

We report a measurement of the dimensionless enhancement factor κ_0 for the Rb-¹²⁹Xe pair commonly used in spin exchange optical pumping (SEOP) to produce hyperpolarized ¹²⁹Xe. κ_0 characterizes the amplification of the ¹²⁹Xe magnetization contribution to the Rb electronic effective field, compared to the case of a uniform continuous medium in classical magnetostatics. The measurement is carried out in Rb vapor cells containing both ³He and ¹²⁹Xe and relies on the previously measured value of κ_0 for the Rb-³He pair. The measurement is based on (1) the optically detected (Faraday rotation) frequency shift of the ⁸⁷Rb electron paramagnetic resonance (EPR) hyperfine spectrum caused by the SEOP nuclear polarization and subsequent sudden destruction of nuclear polarization of both species and (2) a comparison of nuclear magnetic resonance signals for the two species acquired just prior to the EPR frequency shift measurements. We find $(\kappa_0)_{\text{RbXe}} = 518 \pm 8$, in good agreement with previous measurements and theoretical estimates but with improved precision.

DOI: [10.1103/PhysRevA.100.053415](https://doi.org/10.1103/PhysRevA.100.053415)

I. INTRODUCTION

Almost six decades have passed since the first report of a hyperpolarized noble gas [1], but the field continues to grow and evolve, both in terms of the basic physics and the manifold applications. Nuclei of the stable spin- $\frac{1}{2}$ isotopes ³He [2] and ¹²⁹Xe [3] may be polarized by spin-exchange optical pumping (SEOP) [4], a two-stage process of angular momentum transfer. The ground-state electron spins of an alkali-metal vapor are polarized by the absorption of circularly polarized resonant light at the D_1 transition ($5S_{1/2} \rightarrow 5P_{1/2}$ in Rb); subsequent collisions of the polarized alkali-metal atoms with noble gas atoms mediate an interatomic Fermi-contact interaction through which electron and nuclear spin is exchanged. The result is an ensemble of noble-gas atoms with a nuclear-spin polarization in the range of 10–100%, several orders of magnitude beyond the thermal-equilibrium value at room temperature in even the largest laboratory magnetic fields. Hyperpolarized noble gases (in some cases along with a cohabitating polarized alkali-metal vapor) are used in sensitive magnetometry [5], inertial guidance [6], and the search for physics beyond the standard model [7–10]. They are additionally used as a sensitive signal source in magnetic resonance imaging [11,12].

Electron paramagnetic resonance (EPR) of the alkali-metal hyperfine structure can be a sensitive embedded probe of the

magnetic field generated by the evolving noble-gas nuclear magnetization in a SEOP cell. The same Fermi-contact interaction that transfers spin to the noble gas also produces a shift in the alkali-metal EPR frequency ν_A that is proportional to the nuclear magnetization [13]:

$$\Delta|\nu_A| = \frac{1}{h} \frac{8\pi}{3} \left| \frac{d\nu_A}{dB_0} \right| M_X \kappa_{AX}, \quad (1)$$

where the nuclear magnetization M_X is given by

$$M_X = \mu_X \frac{\langle K_z \rangle}{K} [X]. \quad (2)$$

In Eqs. (1) and (2), $[X]$, μ_X , and K are the noble-gas number density, magnetic moment, and spin, respectively; h is Planck's constant, B_0 is the applied magnetic field, and $\kappa_{AX} > 0$ is a dimensionless factor specific to each alkali-metal/noble-gas pair that parametrizes the enhancement of the noble-gas magnetic field sensed by the alkali-metal electrons. The enhanced field results from the quantum mechanical overlap of the electron wave function at the noble-gas nucleus, time-averaged over many collisions. A value of unity for κ_{AX} corresponds to the hypothetical case where the electron classically overlaps a continuous uniform noble-gas magnetization having the same value as that calculated by Eq. (2) for discrete noble-gas atoms. The enhancement is ≈ 5 in the case of Rb-³He [14] and about 500 in the case Rb-¹²⁹Xe [15], owing to xenon's much greater atomic number.

In this paper we present a precise measurement of κ_0 for the Rb-¹²⁹Xe pair; the limit $\kappa_{AX} \rightarrow \kappa_0$ obtains for sufficiently high third-body gas pressure (see Sec. II below). Our measurement

*Present address: Hill Air Force Base, Ogden, Utah 84056, USA

†brian.saam@wsu.edu

is based on a ratiometric comparison of the optically detected ^{87}Rb EPR frequency shifts due to ^{129}Xe and ^3He . Our result, $(\kappa_0)_{\text{RbXe}} = 518 \pm 8$, is in good agreement with a previous measurement, 493 ± 31 , based on the measured ratio of ^{129}Xe and ^3He nuclear magnetic resonance (NMR) frequency shifts [15]. It is also in good agreement with a recent theoretical prediction, 588 ± 50 , based on detailed electronic-structure calculations [16]. A precise measurement of $(\kappa_{AX})_{\text{RbXe}}$ is relevant to better understanding of SEOP physics for the Rb-Xe pair [17] and vital for understanding and correcting systematic shifts in several tests of fundamental symmetries that feature alkali-metal and/or noble-gas magnetometers and comagnetometers [18]. It can also be used to calibrate *in situ* polarimetry of hyperpolarized ^{129}Xe as it is produced by SEOP for the various applications.

II. THEORY

For an applied magnetic field B_0 where the alkali-metal hyperfine splitting is large compared to the electron Zeeman splitting, the effective alkali-metal gyromagnetic ratio for $\Delta m_F = \pm 1$ transitions within the same hyperfine manifold, correct to linear terms in B_0 , is [19]

$$\left. \frac{dv_A}{dB_0} \right|_{I \pm 1/2} = \frac{|g_s| |\mu_B|}{2I + 1} \left(1 \mp \frac{2\bar{m}_F |g_s| |\mu_B|}{A(2I + 1)} B_0 + O(B_0^2) + \dots \right), \quad (3)$$

where I is the alkali-metal nuclear spin, $g_s = -2.0023$ is the free-electron g factor, and A is the alkali-metal hyperfine coupling strength. The total angular momentum quantum number is $F = I \pm 1/2$, corresponding to the two hyperfine manifolds; and \bar{m}_F is the mean value of the two magnetic quantum numbers for the neighboring levels involved in the transition. Equation (3) represents the quadratic Zeeman splitting into $4I$ hyperfine spectral lines, one for each F, \bar{m}_F pair. Under our experimental conditions, a highly polarized vapor means that Rb atoms are pumped into one of the end states $m_F = \pm F$ of the $I + 1/2$ manifold by σ^\pm polarized light.

Spin exchange is mediated through both binary Rb-Xe collisions and the formation of longer-lived RbXe van der Waals molecules [20]. As described in detail by Schaefer *et al.* [13], the enhancement factor may be written as

$$\kappa_{AX} = (\kappa_0 - \kappa_1) + \epsilon_{AX} \kappa_1, \quad (4)$$

where $0 \leq \epsilon_{AX} \leq 1$ characterizes the fractional suppression of the enhancement that occurs as the mean lifetime of RbXe van der Waals molecules increases, i.e., as the mean precession angle ϕ of the coupled angular momenta about the molecular magnetic field during a RbXe van der Waals molecular lifetime approaches and exceeds one radian [21]. At sufficiently large third-body pressure (short molecular lifetime), $\epsilon_{AX} \rightarrow 1$ and $\kappa_{AX} \rightarrow \kappa_0$. According to Zeng *et al.* [21],

$$\phi = \frac{p_0}{p}, \quad (5)$$

where p is the total gas pressure and p_0 is a pressure that depends on gas composition and characterizes the transition from short to long molecular lifetime. For the Cs-Xe pair, $p_0 = 384$ torr if the third-body gas is He [22]; we assume that this number is not very different for the Rb-Xe pair.

TABLE I. Gas composition (in torr at 20 °C) of the three cells used in this work. Cell volume is shown in parenthesis below the cell designation.

	Cell 203C (7.75 cm ³)	Cell 204F (7.61 cm ³)	Cell 205B (7.1 cm ³)
Helium	2185 ± 85	1639 ± 65	2103 ± 80
Xenon	41 ± 2	22 ± 1	18 ± 1
Nitrogen	45 ± 2	34 ± 1	43 ± 2
Total	2271 ± 85	1695 ± 65	2164 ± 80

(For N_2 as the third body, the difference is about 30% [13].) All of our cells contain at least four times this characteristic pressure of He. From Table II by Schaefer *et al.* [13], the ratio $\kappa_1/\kappa_0 \approx 0.08$ for the Rb-Xe pair; from Eq. 8 in Ref. [13], we calculate $\epsilon_{AX} \geq 0.995$ for all of our cells. We conclude that for our experiments the true value of κ_{AX} deviates from κ_0 by less than 0.1% in all cases, and we treat the effect of κ_1 as negligible.

In Rb vapor cells containing both ^3He and ^{129}Xe , one can perform rapid consecutive measurements of the EPR frequency shifts due to each noble-gas species (see Sec. III). From Eq. (1) the ratio of these shifts is

$$\frac{\Delta v_{\text{Xe}}}{\Delta v_{\text{He}}} = \frac{(\kappa_0)_{\text{RbXe}} M_{\text{Xe}}}{(\kappa_0)_{\text{RbHe}} M_{\text{He}}}. \quad (6)$$

The ratio $M_{\text{Xe}}/M_{\text{He}}$ can be determined by NMR measurements of free-induction decay (FID) signals for the two species. Using the previously measured value of $(\kappa_0)_{\text{RbHe}} = 4.52 + 0.00934T$, where T is the temperature in °C [14], Eq. (6) can then be used to determine $(\kappa_0)_{\text{RbXe}}$. Both the EPR frequency shift and the NMR signal intensity depend only on the product of the nuclear polarization and the noble-gas density, i.e., the magnetization M in Eq. (2); therefore, the measurement of $(\kappa_0)_{\text{RbXe}}$ requires no knowledge of the polarization of either noble-gas species and is insensitive to uncertainties in the cell pressures listed in Table I. The accuracy of the measurement comes down to (1) the degree to which we ensure the same initial nuclear magnetization for the EPR and NMR measurements (separately for both ^3He and ^{129}Xe), and (2) the degree to which the recorded measurements of the EPR and NMR signals are proportional to those magnetizations.

III. EXPERIMENT

We performed experiments on three spherical vapor cells of similar volume made of borosilicate (Pyrex) glass; they were filled with several tens of torr of N_2 and Xe gases (the Xe is enriched to 90% ^{129}Xe), about 2000 Torr ^3He , and a few milligrams of Rb (see Table I). The oven temperature for SEOP ranged between 125 °C and 175 °C, as determined by a resistive thermometric device (RTD) affixed directly to the cell, although laser heating likely still caused the actual interior cell temperature to be somewhat warmer. In general, both ^3He and ^{129}Xe were polarized to their respective maximum (saturation) values; we note that this typically took many hours for ^3He and minutes for ^{129}Xe , and that the latter could be polarized at lower temperatures to its saturation value several times in one experiment with little to no effect on the

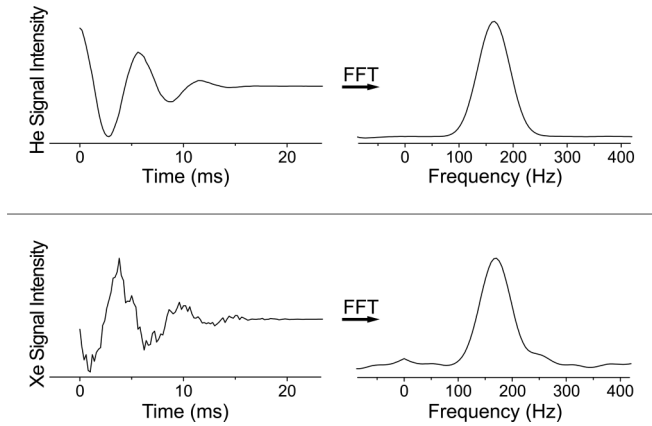


FIG. 1. ^3He (top) and ^{129}Xe (bottom) NMR signals. The left side shows the time-domain free-induction decay (FID) and the right side shows the corresponding Fourier transform relative to the carrier frequency. Signals were acquired at the same frequency (31.25 kHz) with the same RF power and excitation pulse length.

^3He polarization. In all cases, ^3He and ^{129}Xe were polarized into the low-energy Zeeman state using σ^- light. The SEOP pump laser was a 30-watt diode-laser array model A317B (QPC Lasers), externally tuned to the 795 nm D_1 resonance and narrowed to ≈ 0.3 nm with a Littrow cavity [23]. This was an older laser with at least many hundreds of hours of use, and the total output power had deteriorated somewhat; the narrowed output incident on the cell was typically 10–12 W.

Two distinct types of measurements were made:

(1) Separate measurements of the ^3He and ^{129}Xe NMR signal intensities acquired with a Redstone NMR spectrometer (Tecmag); these measurements were made sequentially with a known RF-excitation (flip) angle at one Larmor frequency, adjusting the applied magnetic field B_0 to the corresponding value for each nucleus (see Sec. IV A below); typical data are shown in Fig. 1.

(2) Sequential optically detected (Faraday rotation) EPR measurements of the ^{87}Rb frequency shift made at the same stable value of applied magnetic field (26.5 G), one made after destruction of the ^3He magnetization and one made after destruction of the ^{129}Xe magnetization; the destruction was accomplished with several near- 90° resonant RF pulses from the Redstone spectrometer, which was switched between the respective Larmor frequencies; typical data are shown in Fig. 2.

Figure 3 is a schematic diagram for the entire experiment, showing alignments of the pump and probe lasers, main-field and excitation coils, and the detection and amplification chains for both NMR and EPR.

A. NMR

The NMR probe was a parallel-capacitance-tuned pair of coils (3 cm diameter) separated by about 5 cm, each with multiple layered windings of 25/45 Litz wire (coil inductance was ≈ 30 μH). Since the goal was to measure the signal ratio for ^{129}Xe and ^3He at known flip angles for each nucleus, we sought to eliminate all other sources of instrumental discrepancies and systematic effects by using the same cell,

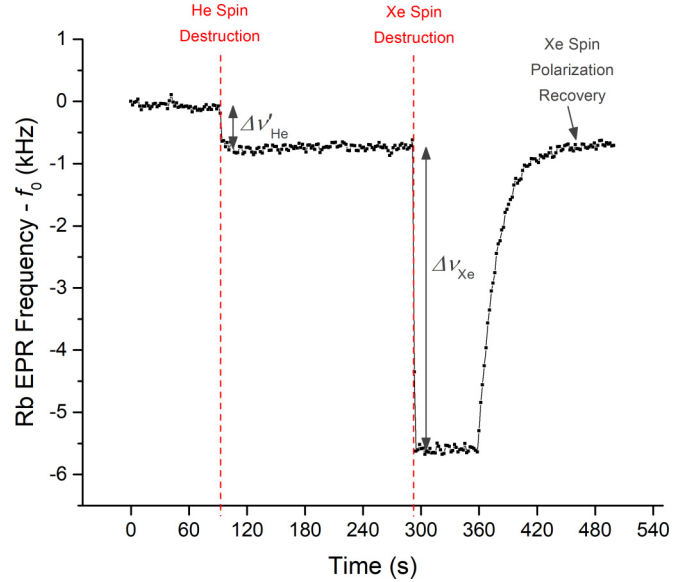


FIG. 2. ^{87}Rb EPR frequency as a function of time, measured relative to the initial recorded frequency $f_0 = 18.6$ MHz in cell 204F at 150°C . At $t = 0$ both ^3He and ^{129}Xe were fully polarized. At ≈ 90 s, the ^3He magnetization was selectively destroyed with a comb of resonant (85.6 kHz) NMR pulses causing a frequency shift $\Delta\nu'_{\text{He}}$. At ≈ 290 s, the ^{129}Xe magnetization was similarly destroyed, yielding a frequency shift $\Delta\nu_{\text{Xe}}$. The ^{129}Xe magnetization recovered in a few minutes to its original value; the ^3He magnetization showed no appreciable recovery throughout the experimental run.

along with the same NMR spectrometer, frequency, probe, and amplifier settings for both measurements. For our operating Larmor frequency of 31.25 kHz, this required adjusting B_0 to 26.5 G for ^{129}Xe and 9.6 G for ^3He . A home-built preamplifier coupled the probe to the spectrometer; signals were displayed and analyzed using the TNMR (Tecmag) software. The spectrometer was also used (in transmit mode only) for rapid destruction of ^{129}Xe and ^3He polarizations at the frequencies 31.25 and 85.6 kHz, respectively, as further discussed in the next section.

B. Optically detected EPR

EPR of ^{87}Rb was optically detected in a manner similar to that described by Chann *et al.* [24], and a double-homodyning scheme was used to lock the EPR frequency to the measured magnetic field. A 80-mW external-cavity-tuned probe laser, model DL-7140-201S (Sanyo), was directed transversely to the main applied magnetic field through the cell and then detected by a fast (2-ns rise time) silicon PIN photodiode, model 54-520 (Edmund Optics). The probe laser was detuned ≈ 1 nm from the ^{87}Rb D_2 resonance at 780 nm, where Faraday rotation of the plane of polarization has a well-characterized linear dependence on the ^{87}Rb spin polarization along the propagation axis of the probe beam. The probe-beam diameter is a few millimeters, which is small compared to the cell diameter. A weak cw RF excitation generated a steady-state precessing transverse ^{87}Rb magnetization at frequencies corresponding to the hyperfine resonances (≈ 19 MHz at 26.5 G for ^{87}Rb). The resonance intensity at each hyperfine frequency

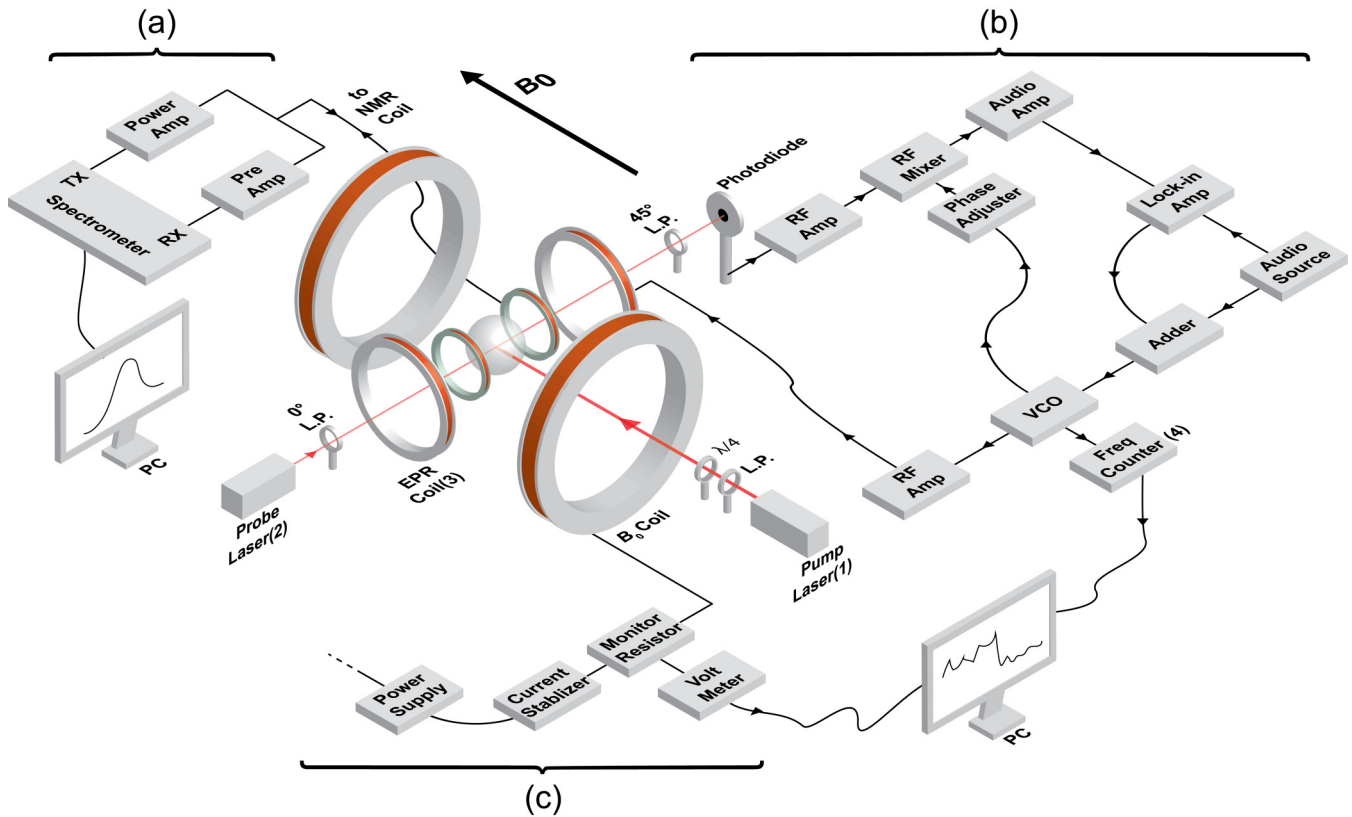


FIG. 3. Schematic of experimental apparatus; model/manufacturer designations not noted here appear in the text. (a) The NMR spectrometer transmits excitation pulses to and receives the subsequent FID signal from a tuned coil placed near the cell. (b) Optically detected EPR consists of (1) The 795 nm pump laser with 10–12 W of power narrowed to ~ 0.3 nm. (2) An 80-mW probe laser detuned by ≈ 1 nm that probes the Rb magnetization via Faraday rotation; the transmitted light (intensity modulated at the ≈ 19 MHz EPR frequency) is focused onto a fast photodiode. (3) A two-turn tuned EPR coil, located coaxially but outside the NMR coil, is driven by a voltage-controlled oscillator (VCO) through a ZHL-32A RF amplifier (Mini-Circuits). The ZAD-1 RF mixer (Mini-Circuits) homodynes the photodiode signal with the VCO output; the difference signal is fed to a model 186A lock-in amplifier (Princeton Applied Research) referenced to a 100-Hz sine wave that also modulates the VCO frequency with an amplitude much smaller than the transition linewidth. The derivative (error) signal at the lock-in output locks the frequency to the peak of the ^{87}Rb hyperfine resonance. (4) A precision counter records the output frequency from the VCO and sends it to a PC-type computer running a LABVIEW program for display and analysis. (c) The applied magnetic field (26.5 G) is generated by a 60-cm-diam. Helmholtz pair, the current stabilizer described in Fig. 5, and a $0.10\text{-}\Omega$ monitor resistor. The voltage across the monitor resistor is used to correct the residual long-term current drift.

was measured by converting the light-polarization modulation to a light-intensity modulation: a linear polarizer oriented at 45° to the nominal plane polarization of the probe laser was placed in front of the photodiode detector. The detector output was homodyned with the RF source, a voltage-controlled oscillator (VCO), model 80 (Wavetek). The VCO could be swept with a voltage ramp across all of the resonances to generate the full hyperfine spectrum, where we note that the spectrum under optical pumping conditions is asymmetric: most of the intensity resides in the $F = 2$ end resonance that corresponds to the helicity of the D_1 pumping light; see Fig. 4. Operating the VCO with a low-frequency (≈ 100 Hz) modulation having an amplitude small compared to the resonance width generated the derivative of the more intense end resonance; the homodyned photodetector output was fed to a lock-in amplifier (model 186A, Princeton Applied Research) referenced to the modulation frequency; see Fig. 3. The zero crossing of the derivative signal at the resonance peak was used in a loop fed back to the VCO to lock the EPR frequency,

which was read out on a precision frequency counter, model 53220A (Agilent). In an otherwise stable applied field, the locking circuit could reproducibly follow both gradual and sudden changes in the noble-gas nuclear magnetization.

C. Stabilization of applied magnetic field

The measured EPR frequency shifts due to nuclear polarization were 1–10 kHz; we thus needed to stabilize the applied magnetic field B_0 to much better than a part in 10^4 . This was accomplished with the home-built current-stabilization circuit designed by one of us (M.S.C.) and shown in Fig. 5. Most commercial DC power supplies have some difficulty driving inductive loads in current-control mode. The supply used here (model 6267B; Hewlett-Packard) was run in voltage-control mode in series with a power MOSFET and a 250 W $0.5\ \Omega$ resistor (Vishay-Dale) having a temperature coefficient of $10\ \text{ppm}/^\circ\text{C}$. The resistor was immersed in mineral oil for better thermal stability. The current through the MOSFET,

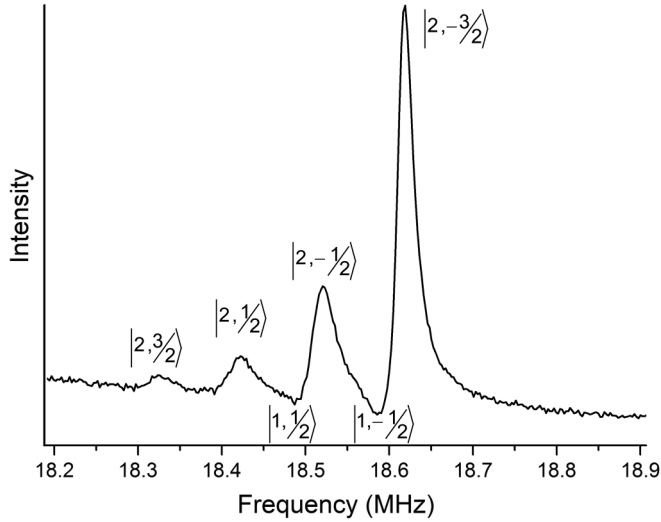


FIG. 4. Optically detected ^{87}Rb EPR hyperfine spectrum under optical pumping conditions at 26.5 G from cell 204A; peaks are labeled by $|F, \bar{m}_F\rangle$. A voltage-controlled oscillator (VCO) swept with a wide voltage ramp across the resonances generates the full hyperfine spectrum. Here, most of the intensity resides in the $F = 2$, $\bar{m}_F = -3/2$ transition, because the σ^- pumping light drives population towards the $|2, -2\rangle$ state. The $F = 1$ transitions are barely discernible (180° out of phase with $F = 2$) to either side of the $|2, -3/2\rangle$ peak.

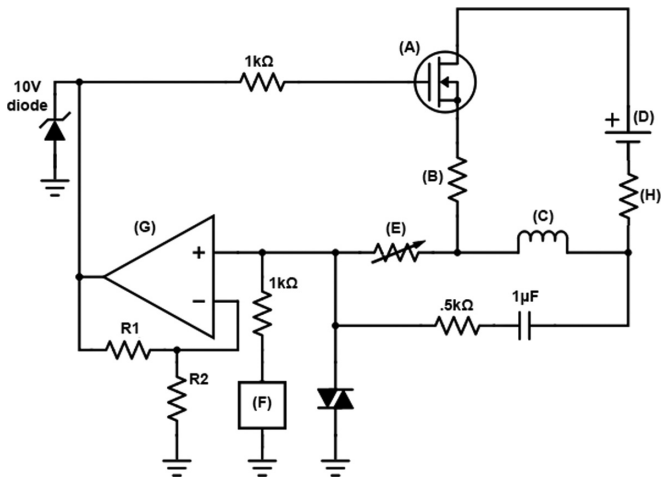


FIG. 5. Current-stabilizing circuit design: a power MOSFET (A) (IRL2910) is placed in series with a high-power shunt resistor (B) (Vishay-Dale 250 W, 0.5 Ω , 100 ppm/ $^\circ\text{C}$) and a high-precision variable resistor (E) (Vishay Accutrim 1240, 0–500 Ω , 10 ppm/ $^\circ\text{C}$). The shunt resistor is submerged in mineral oil to increase thermal mass and minimize temperature change due to air flow. The voltage across the resistors is compared to a stable voltage reference (F) (MAX6341) and fed into the gate terminal of the transistor through a noninverting OP-27 operational amplifier (G) in a negative-feedback mode. The gate voltage controls the drain-source current, which is approximately the same as the one flowing through the coils (C). The 1- μF capacitor is used to damp any current oscillation from the coils. The crossed diodes are used to protect the op-amp. (H) The 0.10- Ω sensing resistor (H) is used to correct the current drifts.

running well out on the flat portion of the I - V_{DS} curve, was controlled via the gate input generated by comparing the voltage across the 0.5 Ω resistor with a stable voltage reference, thus stabilizing the current through the Helmholtz coils. The Helmholtz-coil current was additionally monitored with a precision digital multimeter (model 2000, Keithley) measuring the voltage across a 0.10 Ω stable resistor in series with the coils only. The monitored stabilized current was used to correct for baseline drifts in frequency-shift data acquired over long time periods (many tens of minutes to hours). By running at certain times in the day (usually in the middle of the night) and employing these field-stabilization and monitoring schemes, the rms frequency noise (typically integrated over 1.5 seconds) was reduced to ≤ 100 Hz, or about one part in 2×10^5 of the EPR frequency. Data were acquired and stored with the help of LABVIEW software (National Instruments) on a PC-type computer.

IV. RESULTS AND ANALYSIS

An experimental run consisted of (1) a NMR flip-angle measurement, (2) a measurement of the relative intensity of ^{129}Xe and ^3He NMR signals, and (3) a measurement of the relative size of the corresponding ^{87}Rb EPR resonance shifts due to the ^{129}Xe and ^3He magnetizations.

A. Flip-angle measurement

At some time after both ^3He and ^{129}Xe polarizations had reached their maximum (saturation) values (>20 h of SEOP), we started an experimental run by measuring the magnetization ratio with NMR at 31.25 kHz. The measured initial height S of the free-induction decay (FID) is proportional to the longitudinal magnetization from which it was generated through excitation at some flip angle θ . The magnetization ratio just prior to excitation is given by

$$\frac{M_{\text{Xe}}}{M_{\text{He}}} = \frac{S_{\text{Xe}} \sin \theta_{\text{He}}}{S_{\text{He}} \sin \theta_{\text{Xe}}}. \quad (7)$$

Had we been able to operate in the regime where $\theta \ll 1$ radian for both nuclei, then the sine ratio in Eq. (7) could be replaced by a factor of the ratio of gyromagnetic ratios $\gamma_{\text{He}}/\gamma_{\text{Xe}}$ [25], but this was not the case, and we had to carry out frequent and precise measurements of the flip angles used. This was done in a separate measurement by polarizing the ^3He to saturation and then applying a long series of identical 80- μs pulses at 31.25 kHz, spaced 55 ms apart. The FID acquired after each pulse was Fourier transformed and the area under the peak was measured; see Fig. 6. The magnetization after the n th pulse was

$$M(n) = M_0 \cos^n \theta = M_0 e^{n \ln(\cos \theta)}, \quad (8)$$

Defining $b \equiv \ln(\cos \theta)$, we fit data such as that shown in Fig. 6 to the function ae^{bn} with fitting parameters a and b and then calculated

$$\theta = \arccos(e^b). \quad (9)$$

Provided we used all of the same electronics and the exact same gains and other settings, the ^{129}Xe flip angle was found

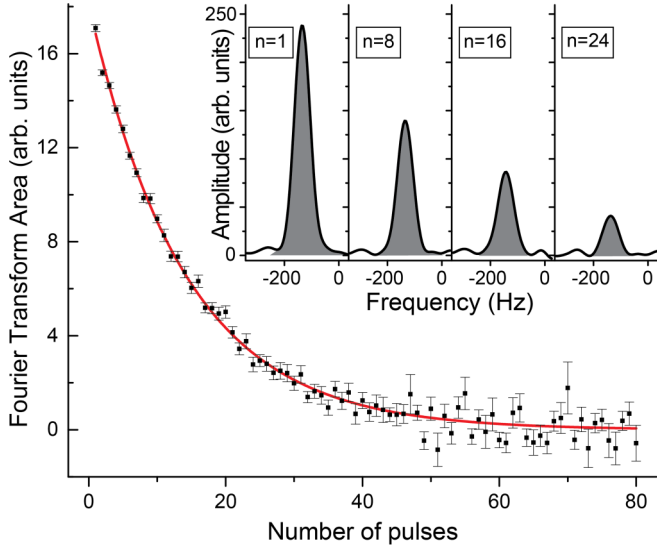


FIG. 6. Signal intensity as a function of pulse number for eighty consecutive $80\text{-}\mu\text{s}$ pulses at the ^3He Larmor frequency, 31.25 kHz ; the rate is one pulse every 55 ms . The ^3He FID after each pulse is collected, digitized, and Fourier transformed. The peak area is plotted vs the number n of pulses and fit to an exponential decay (red line); see Eq. (8).

from

$$\theta_{\text{Xe}} = \frac{\gamma_{\text{Xe}}}{\gamma_{\text{He}}} \theta_{\text{He}}. \quad (10)$$

The output of the NMR pulse amplifier was monitored with an oscilloscope before and after every NMR measurement to ensure that the pulse characteristics in the flip-angle measurement remained consistent over the course of the entire experimental run.

B. NMR signal acquisition

The ^{129}Xe NMR signal in our cells, particularly at low flip angles, is quite weak but recovers in minutes with SEOP. The ^3He signal is strong but needs tens of hours to recover if destroyed. The EPR frequency shifts from ^3He are also smaller than those for ^{129}Xe . We needed to choose a ^3He flip angle low enough to record the NMR signal and still have plenty of magnetization left to record a significant EPR frequency shift when the remaining magnetization was destroyed. If we wanted to use the exact same pulse (frequency, power, and duration) for both species, we thus needed to acquire the ^{129}Xe FID at an even smaller flip angle and then average many such acquisitions.

Starting at full polarization for both ^3He and ^{129}Xe and with the SEOP pump laser on continuously, we applied $N = 100$ pulses 50 ms apart at the ^{129}Xe Larmor frequency of 31.25 kHz in a field $B_0 = 26.5\text{ G}$. The acquired FIDs were added together and Fourier transformed. We assumed that there was no significant additional polarization created by SEOP during the total acquisition time of 5 s ; see Sec. V. Due to the magnetization destroyed after each pulse, the total measured signal $S_N = \sum_{n=1}^N S_n$ needed correction to represent

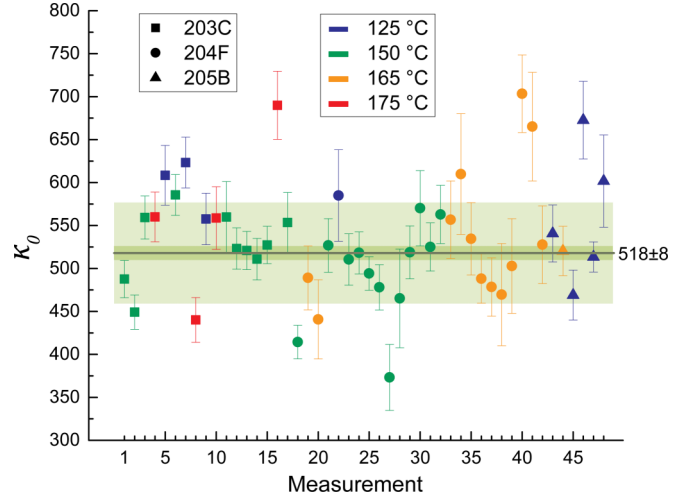


FIG. 7. Calculated values of κ_0 with the corresponding error bars from 48 measurements of three cells at four temperatures. The uncertainty-weighted average of κ_0 with its standard error is shown (dark green band) along with the weighted standard deviation ($\pm 518 \pm 8$) for the whole set of data (light green band).

the signal S_{Xe} after the first measurement:

$$S_{\text{Xe}} = \frac{S_N}{\sum_{n=0}^{N-1} \cos^n \theta}. \quad (11)$$

Immediately after this series of ^{129}Xe NMR signal acquisitions, the applied field was lowered to 9.6 G by reducing the current in the power supply, corresponding to a ^3He Larmor frequency of 31.25 kHz . A single $80\text{-}\mu\text{s}$ excitation pulse was applied, and S_{He} was immediately recorded for ^3He without signal averaging. The pulse length, frequency, and power were unchanged between the ^3He and ^{129}Xe NMR measurements, as were the amplifier gain settings on the receiver side.

C. EPR frequency shift acquisition

After the NMR measurements, the ^{129}Xe magnetization was allowed to recover by SEOP (typically requiring no more than a few minutes). The applied magnetic field was returned to 26.5 G and stabilized using optically detected ^{87}Rb EPR, as described in Sec. III B. A baseline EPR frequency was established prior to destroying the remaining ^3He magnetization with a rapid series of large-angle pulses at 85.6 kHz . A new baseline was then established and the total shift $\Delta\nu'_{\text{He}}$ was recorded. We use the prime because this shift still had to be corrected for the magnetization lost from the one pulse used previously to acquire a single FID:

$$\Delta\nu_{\text{He}} = \frac{\Delta\nu'_{\text{He}}}{\cos \theta_{\text{He}}}. \quad (12)$$

The ^3He magnetization, once destroyed, did not recover to any significant degree during the remainder of the experimental run due to the low spin-exchange rate; this was verified at the very end of the run by repeating the above steps and noting no significant frequency shift.

A few minutes after the ^3He measurement, the ^{129}Xe polarization was similarly destroyed with a series of pulses at 31.25 kHz . Because the ^{129}Xe magnetization recovered

TABLE II. Number of measurements (in bold) shown with the uncertainty-weighted average (with the standard deviation of the mean) of $(\kappa_0)_{\text{RbXe}}$ for each cell at each temperature measured.

	125 °C	150 °C	165 °C	175 °C	Average
Cell 203C	3 596 ± 21	10 519 ± 13		4 537 ± 49	17 532 ± 14
Cell 204F	1 585 ± 53	12 490 ± 15	12 523 ± 21		25 501 ± 12
Cell 205B	5 527 ± 26		1 520 ± 29		6 526 ± 22
Average	9 551 ± 20	22 505 ± 10	13 523 ± 19	4 537 ± 49	48 518 ± 8

quickly via SEOP (within 3 min), we repeat its destruction and recovery five times for each experimental run, averaging the results to obtain the ^{129}Xe frequency shift $\Delta\nu_{\text{Xe}}$; this shift requires no correction, since the starting point is full polarization prior to each destructive series of pulses; see Fig. 2.

There were a total of 48 experimental runs with three different sample cells (Table I) and four different temperatures. The value of κ_0 for RbXe and associated uncertainty was calculated using Eq. (6) for each run; results are shown in the plot in Fig. 7. Table II shows the uncertainty-weighted average values categorized according to both temperature and the sample cell used. The weighted average value for all measurements yields $(\kappa_0)_{\text{RbXe}} = 518 \pm 8$ (green line in Fig. 7), where 8 is the standard deviation of the mean (dark green region) and the light green region (± 59) corresponds to the sample standard deviation.

V. DISCUSSION AND CONCLUSION

There appears to be little correlation of the measured value of κ_0 with the three different cells used. Cell 204F has the lowest total pressure and a 5% smaller value for κ_0 than the other two cells. As discussed in Sec. II, we would not expect this to be due to κ_1 in Eq. (4), as there is enough total gas pressure in all of these cells to assure that the van der Waals molecules are in the short-lifetime limit [20]. Any temperature dependence would appear to be weak at best; this is not unexpected due to the steep core wall of the RbXe van der Waals potential and the strong dependence of the contact interaction on the distance of closest approach. Looking at the overall scatter in the data, the 1.5% relative uncertainty in the weighted average may be a bit optimistic. If so, the source of any systematic error is likely to come from the NMR ratio measurement, since the frequency-shift measurements have better signal-to-noise ratio and involve less post-processing to arrive at the ^{129}Xe - ^3He signal ratio. Despite our careful efforts to calibrate the NMR equipment, drifts in sensitivity during the measurements due to thermally sensitive components or to inhomogeneities in the transverse excitation field cannot be completely ruled out.

In Sec. IV B, we assumed that no additional ^{129}Xe nuclear polarization is generated by SEOP during the ≈ 5 s interval over which ^{129}Xe NMR signals are rapidly acquired and

averaged. To justify this assumption, we use the known binary spin-exchange rate coefficient $k_{\text{se}} = 2.2 \times 10^{-16} \text{ cm}^3/\text{s}$ for Rb- ^{129}Xe [26] and the Rb vapor pressure curve due to Killian [27] to estimate the spin-exchange time γ_{se}^{-1} to be in range 13–170 s for the temperature range $T = 175$ – 125 °C. The wall-relaxation time Γ_w^{-1} in these cells is a few minutes or more, so most of our measurements (e.g., the one shown in Fig. 2) well satisfy $\tau_{\text{up}} \gg 5$ s, where the “spin-up” time $\tau_{\text{up}} = (\gamma_{\text{se}} + \Gamma_w)^{-1}$. Moreover, since the flip angle $\theta_{\text{Xe}} \ll 1$ rad, many if not most of the acquisitions over the 5-s interval occur near the steady-state polarization maximum, where the slope of the spin-exchange transient is smallest and the corresponding polarization recovery is weakest.

We further assumed for both the EPR and NMR measurements that the nuclear magnetization is uniform throughout the cell for both nuclear species at the time any measurement is initiated. The relevant diffusion coefficients [28,29] are such that ^3He atoms traverse these cells in a characteristic time τ_d of a few seconds at most and that Xe atoms do so in no more than about 10–15 s. Since the condition $\tau_d \ll \tau_{\text{up}}$ always holds for ^3He , there is never a question that the ^3He magnetization is uniform. The same condition usually also holds for ^{129}Xe , although at our highest measurement temperatures it may only be marginally satisfied. Nevertheless, if the cell is approximately uniformly illuminated and the initial EPR frequency measurement (prior to polarization destruction) is made after several times τ_{up} , any residual nuclear polarization gradient in the cell should be very small. Thus, for the few measurements made at the highest temperatures, there may have been some very small amount of recovery during the ^{129}Xe NMR acquisition, as well as a small ^{129}Xe polarization gradient, but there are no obvious trends in the data at high temperatures to suggest that we cannot ignore both of these effects.

Another systematic effect we considered was cell asphericity: both the slightly oblate or prolate shape of the nominally spherical cell and the “pull-off,” the roughly cylindrical sub-volume protruding radially out from the main cell volume. The pull-off is formed as a byproduct of flame-sealing the cell away from a glass manifold after it has been filled with a few tens of milligrams of alkali metal and the constituent gases. A perfectly spherical distribution of a uniformly magnetized material produces zero through-space field in the interior of the sphere. Asphericity produces a net nonzero through-space field which would also be probed by the EPR laser, producing a frequency shift that cannot be distinguished from that due to the Fermi-contact interaction. We find that the effects of asphericity contribute at no more than about the 0.4% to our results, significantly smaller than our quoted statistical error; details are discussed in the Appendix.

With appropriate rearrangement of Eqs. (1) and (2), our result can be used to calibrate the measured EPR frequency shift to the absolute ^{129}Xe polarization $P_{\text{Xe}} = \langle K_z \rangle / K$. This relationship also shows that the largest measured EPR shifts in our cells, combined with knowledge of the Xe density, sets a lower bound for $(\kappa_0)_{\text{RbXe}}$. In the case of these measurements, a maximum shift of 5.0 kHz was recorded for cell 204F, yielding a ^{129}Xe polarization of 87% using our measured value of $(\kappa_0)_{\text{RbXe}}$; alternatively, by assuming 100% polarization, the measurement of that same shift sets a lower bound on $(\kappa_0)_{\text{RbXe}}$ of 452.

To put our measurement into context with those preceding it, we first note that the result agrees well statistically with the results of Ma *et al.* [15], who measured $(\kappa_0)_{\text{RbXe}} = 493 \pm 30$ using an entirely different experimental method (comparing the NMR frequency shifts for ^3He and ^{129}Xe in the presence of a polarized Rb vapor), although they similarly relied on the previous κ_0 result for Rb- ^3He [14]. The present result is somewhat smaller than the recent theoretical/computational results of Hanni *et al.* [16] who determined $(\kappa_0)_{\text{RbXe}} = 588 \pm 50$; but the discrepancy is not alarming considering the uncertainties. Earlier estimates by Walker [30] and measurements by Schaefer *et al.* [13] were in the range of 650 to 750, but had much larger uncertainties, and so are also not inconsistent with our result. Finally, we note that this work may be relevant to SEOP of radon for measurements of the permanent electric-dipole moment (EDM) [7,31,32]; radon is a strong candidate for observing a nonzero EDM and/or setting the best experimental limit on its value. The enhancement factor κ_0 is predicted to be as large as 1400 for the Rb-Rn system [30]; the effects of the associated frequency shifts may thus play a significant role in these precision measurements.

ACKNOWLEDGMENTS

The authors thank University of Utah glassblower K. Teaford for cell and sample chamber manufacturing and acknowledge the US National Science Foundation Grant No. PHY-1708048 for support of this work.

APPENDIX: EFFECTS OF CELL ASPHERICITY

Here we estimate the effects of having imperfectly spherical cells. Since $(\kappa_0)_{\text{RbHe}} \approx 5$ is on the order of unity and much smaller than $(\kappa_0)_{\text{RbXe}}$, the nonzero through-space field in nonspherical geometries can be an important systematic effect in deducing the correct EPR frequency shift and relating it to κ_0 . Since the effect produces a much larger fractional change in $(\kappa_0)_{\text{RbHe}}$, we treat any fractional systematic error in the measurement of the EPR shift due to ^3He as the fractional error in the ratio measurement. We start with (in Gaussian units)

$$\mathbf{B} = \mathbf{H} + 4\pi\mathbf{M} \quad (\text{A1})$$

and recall that the δ -function contribution to the field in any magnetized region is given by $\mathbf{B}_\delta = \frac{8\pi}{3}\mathbf{M}$. We consider two possible sources of these effects: global asphericity of the cell and the cell pull-off.

1. Modeling the pull-off

Figure 8 shows an idealized drawing of a spherical vapor cell with a cylindrical pull-off with relevant dimensions given in units of the cell radius R . In our experiments the pull-off was oriented toward the floor, and the applied field was horizontal, as depicted in the figure. The total magnetic moment inside the cylindrical pull-off is $\mu_{\text{cyl}} = \pi a^2 b R^3 M_0$, where M_0 is the uniform magnetization of the cell, aR is the pull-off radius, and bR is the pull-off length. We consider the through-space field at the center of the cell, although the narrow (relative to R) probe laser beam nominally runs along a line through the cell center; the field will thus be a little

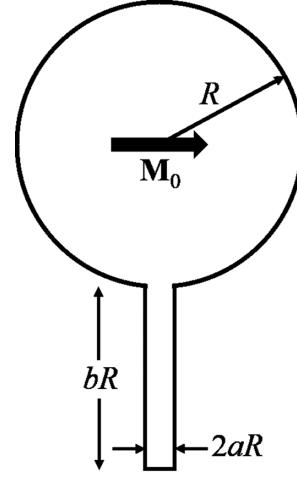


FIG. 8. Vapor cell idealized as a perfect sphere connected to a cylinder that models the cell pull-off.

smaller as one approaches the entrance and exit points of the probe beam.

As a first crude approximation, we assume that the total magnetic moment of the pull-off is a point dipole located in the middle of the pull-off, i.e., that it is $R + \frac{1}{2}bR$ away from the center of the cell. This will generate a field B_{pull} at the cell center given by

$$B_{\text{pull}} = -\frac{\mu_{\text{cyl}}}{R^3(1 + \frac{1}{2}b)^3} = -\frac{\pi a^2 b}{(1 + \frac{1}{2}b)^3} M_0, \quad (\text{A2})$$

where the negative sign indicates that \mathbf{B}_{pull} is antiparallel to the magnetization \mathbf{M}_0 . For typical values in the cells used in this work, $a = 0.2$, $b = 1.2$, $B_{\text{pull}} = -0.037M_0$.

A better approximation assumes a uniform line of dipoles occupies the pull-off with linear magnetization density $\pi a^2 R^2 M_0$; we then integrate the pull-off field from $z = R$ to $z = (1 + b)R$:

$$B_{\text{pull}} = -\int_R^{R(1+b)} \frac{\pi a^2 R^2}{z^3} M_0 dz = \frac{\pi a^2}{2} \left[\frac{1}{(1+b)^2} - 1 \right] M_0. \quad (\text{A3})$$

For the same values of a and b , we now obtain $B_{\text{pull}} = -0.050M_0$. As expected, the magnitude of this estimate is larger than the first one due to the $1/r^3$ drop-off of the dipolar field. If we divide our result by the contact field $\frac{8\pi}{3}(\kappa_0)_{\text{RbHe}}M_0 \approx 40M_0$, it translates directly to a fractional error in our ratio measurement, meaning that the pull-off might systematically depress the measured value of $(\kappa_0)_{\text{RbXe}}$ at about the 0.1% level, a small change compared to our quoted statistical error.

2. Modeling global asphericity

The through-space field is uniform and nonzero for uniformly magnetized ellipsoids. We model the global cell asphericity as a slight difference in major axis along one of the coordinate axes—in other words, as an oblate or prolate spheroid—and calculate the slight deviation of the interior through-space field from zero. The general calculation is not trivial; a good reference is due to Osborn [33]. The

demagnetizing tensor \mathcal{N} is defined by

$$\mathbf{H}_d = -4\pi\mathcal{N} \otimes \mathbf{M}, \quad (\text{A4})$$

where \mathbf{H}_d is the value of the magnetic field (H field) that produces the correct magnetic induction (B field) in a given magnetized geometry. In highly symmetric situations with uniform magnetization, the tensor is diagonalized to values along the three principal axes, N_x , N_y , and N_z . For a sphere magnetized along the z axis, $N_z = 1/3$, yielding the result that the B field inside the sphere is due entirely to the δ -function contribution.

Osborn [33] calculated the principal demagnetizing factors for a general ellipsoid with principal axes a , b , and c along the x -, y -, and z -coordinate axes, respectively. We reproduce here his results for the special cases of prolate and oblate spheroids with the symmetry axis in the z direction. For a prolate spheroid ($c > a$, $a = b$), with $m \equiv c/a$:

$$N_z^p = \frac{1}{m^2 - 1} \left[\frac{m}{2\sqrt{m^2 - 1}} \ln \left(\frac{m + \sqrt{m^2 - 1}}{m - \sqrt{m^2 - 1}} \right) - 1 \right], \quad (\text{A5})$$

whereas, for an oblate spheroid ($c < a$, $a = b$, $m \equiv c/a$),

$$N_z^o = \frac{1}{1 - m^2} \left[1 - \frac{m}{\sqrt{1 - m^2}} \arcsin \sqrt{1 - m^2} \right]. \quad (\text{A6})$$

We consider a 5% difference in major axes: for $c/a = 1.05$ we obtain $N_z^p = 0.32042$ and for $a/c = 1.05$ we obtain $N_z^o = 0.34643$. The resulting nonzero through-space B field produced in our cells by these demagnetizing factors is

$$B_z^{\text{bs}} = 4\pi \left(\frac{1}{3} - N_z \right) M_0. \quad (\text{A7})$$

Equation (A7) yields $B_z^{\text{bs}} = \pm 4\pi(0.0129)M_0$ for the prolate (oblate) spheroid. If we again divide these results by the contact field $\frac{8\pi}{3}(\kappa_0)_{\text{RbXe}}M_0 \approx 40M_0$, the corresponding systematic contribution to the measured value of $(\kappa_0)_{\text{RbXe}}$ occurs at about the 0.4% level. We also note that whereas any effect due to the pull-off acts to depress the value of $(\kappa_0)_{\text{RbXe}}$, the sign of the effect for global asphericity depends on whether the cell is prolate or oblate.

-
- [1] M. A. Bouchiat, T. R. Carver, and C. M. Varnum, *Phys. Rev. Lett.* **5**, 373 (1960).
- [2] T. R. Gentile, P. J. Nacher, B. Saam, and T. G. Walker, *Rev. Mod. Phys.* **89**, 045004 (2017).
- [3] *Hyperpolarized Xenon-129 Magnetic Resonance: Concepts, Production, Techniques and Applications*, edited by T. Meersmann and E. Brunner (Royal Society of Chemistry, Cambridge, 2015).
- [4] T. G. Walker and W. Happer, *Rev. Mod. Phys.* **69**, 629 (1997).
- [5] M. E. Limes, D. Sheng, and M. V. Romalis, *Phys. Rev. Lett.* **120**, 033401 (2018).
- [6] T. Walker and M. Larsen, in *Spin-Exchange Pumped NMR Gyros*, edited by E. Arimondo, C. C. Lin, and S. F. Yelin (Academic, New York, 2016), Vol. 65, Chap. 8.
- [7] T. E. Chupp, P. Fierlinger, M. J. Ramsey-Musolf, and J. T. Singh, *Rev. Mod. Phys.* **91**, 015001 (2019).
- [8] J. Lee, A. Almasi, and M. Romalis, *Phys. Rev. Lett.* **120**, 161801 (2018).
- [9] F. Kuchler, E. Babcock, M. Burghoff, T. Chupp, S. Degenkolb, I. Fan, P. Fierlinger, F. Gong, E. Kraegeloh, W. Kilian, S. Knappe-Grüneberg, T. Lins, M. Marino, J. Meinel, B. Niessen, N. Sachdeva, Z. Salhi, A. Schnabel, F. Seifert, J. Singh, S. Stüber, L. Trahms, and J. Voigt, *Hyperfine Interact.* **237**, 95 (2016).
- [10] F. Allmendinger, W. Heil, S. Karpuk, W. Kilian, A. Scharth, U. Schmidt, A. Schnabel, Y. Sobolev, and K. Tullney, *Phys. Rev. Lett.* **112**, 110801 (2014).
- [11] J. P. Mugler and T. A. Altes, *J. Magn. Reson. Imaging* **37**, 313 (2013).
- [12] J. C. Leawoods, D. A. Yablonskiy, B. Saam, D. S. Gierada, and M. S. Conradi, *Concepts Magn. Reson.* **13**, 277 (2001).
- [13] S. R. Schaefer, G. D. Cates, T.-R. Chien, D. Gonatas, W. Happer, and T. G. Walker, *Phys. Rev. A* **39**, 5613 (1989).
- [14] M. V. Romalis and G. D. Cates, *Phys. Rev. A* **58**, 3004 (1998).
- [15] Z. L. Ma, E. G. Sorte, and B. Saam, *Phys. Rev. Lett.* **106**, 193005 (2011).
- [16] M. Hanni, P. Lantto, M. Repisky, J. Mareš, B. Saam, and J. Vaara, *Phys. Rev. A* **95**, 032509 (2017).
- [17] A. Korver, D. Thrasher, M. Bulatowicz, and T. G. Walker, *Phys. Rev. Lett.* **115**, 253001 (2015).
- [18] J. C. Allred, R. N. Lyman, T. W. Kornack, and M. V. Romalis, *Phys. Rev. Lett.* **89**, 130801 (2002).
- [19] G. Breit and I. I. Rabi, *Phys. Rev.* **38**, 2082 (1931).
- [20] W. Happer, E. Miron, S. Schaefer, D. Schreiber, W. A. van Wijngaarden, and X. Zeng, *Phys. Rev. A* **29**, 3092 (1984).
- [21] X. Zeng, Z. Wu, T. Call, E. Miron, D. Schreiber, and W. Happer, *Phys. Rev. A* **31**, 260 (1985).
- [22] J. Hsu, Z. Wu, and W. Happer, *Phys. Lett. A* **112**, 141 (1985).
- [23] B. Chann, I. Nelson, and T. G. Walker, *Opt. Lett.* **25**, 1352 (2000).
- [24] B. Chann, E. Babcock, L. W. Anderson, and T. G. Walker, *Phys. Rev. A* **66**, 032703 (2002).
- [25] B. T. Saam and M. S. Conradi, *J. Magn. Reson.* **134**, 67 (1998).
- [26] Y.-Y. Jau, N. N. Kuzma, and W. Happer, *Phys. Rev. A* **67**, 022720 (2003).
- [27] T. Killian, *Phys. Rev.* **27**, 578 (1926).
- [28] R. Barbé, M. Leduc, and E. Laloë, *J. Phys. (Paris)* **35**, 935 (1974).
- [29] R. H. Acosta, L. Agulles-Pedros, S. Komin, D. Sebastiani, H. W. Spiess, and P. Blümler, *Phys. Chem. Chem. Phys.* **8**, 4182 (2006).
- [30] T. G. Walker, *Phys. Rev. A* **40**, 4959 (1989).
- [31] E. R. Tardiff, E. T. Rand, G. C. Ball, T. E. Chupp, A. B. Garnsworthy, P. Garrett, M. E. Hayden, C. A. Kierans, W. Lorenzon, M. R. Pearson, C. Schaub, and C. E. Svensson, E. R. Tardiff, E. T. Rand, and G. C. Ball, *Hyperfine Interact.* **225**, 197 (2014).
- [32] M. Kitano, F. P. Calaprice, M. L. Pitt, J. Clayhold, W. Happer, M. Kadar-Kallen, M. Musolf, G. Ulm, K. Wendt, T. Chupp, J. Bonn, R. Neugart, and E. Otten, and H. T. Duong, *Phys. Rev. Lett.* **60**, 2133 (1988).
- [33] J. A. Osborn, *Phys. Rev.* **67**, 351 (1945).